Unconventional spin-orbit torques from sputtered MoTe$_2$ films

Shuchen Li,[1,*] Jonathan Gibbons,[1,2] Stasiu Chyczewski ®,[3] Zetai Liu,[3] Hsu-Chih Ni ®,[1] Jiangchao Qian ®,[1] Jian-Min Zuo,[1] Jun-Fei Zheng,[4] Wenjuan Zhu,[3] and Axel Hoffmann[1,†]

[1]*Department of Materials Science and Engineering and Materials Research Laboratory,*
University of Illinois Urbana-Champaign, Urbana, Illinois 61801, USA
[2]*Department of Physics, University of California–San Diego, La Jolla, California 92093, USA*
[3]*Department of Electrical and Computer Engineering, University of Illinois Urbana-Champaign, Urbana, Illinois 61801, USA*
[4]*Entegris Inc., Danbury, Connecticut 06810, USA*

Materials with strong spin-orbit coupling and low crystalline symmetry are promising for generating large unconventional spin-orbit torques (SOTs), such as in-plane fieldlike (FL) torques and out-of-plane dampinglike (DL) torques, which can effectively manipulate and deterministically switch an out-of-plane magnetization without the need for additional external in-plane magnetic fields. Here, we report SOTs generated by magnetron-sputtered $1T'$ MoTe$_2$/Permalloy (Py; Ni$_{80}$Fe$_{20}$)/MgO heterostructures using both spin-torque ferromagnetic resonance (ST-FMR) and second harmonic Hall measurements. We observed unconventional FL and DL torques in our samples due to spins polarized normal to the interface of MoTe$_2$ and Py layers, and studied the influence of crystallographic order and MoTe$_2$ layer thickness on the SOTs. By comparing the Raman spectra of $1T'$ MoTe$_2$ samples prepared in different ways, we found a tensile strain in sputtered MoTe$_2$ films, which might further enhance the generation of unconventional torques by reducing the symmetry of $1T'$ MoTe$_2$.

I. INTRODUCTION

Spin-orbit torques (SOTs) are promising for novel information technologies, such as nonvolatile magnetoresistive random-access memory [1–3] as they can efficiently manipulate magnetization dynamics by transferring angular momentum to the magnetic thin films [4] with demonstrated low power (130 pJ) and high speed (210 ps) [5]. When applying a charge current through the spin source material, which has large spin-orbit couplings, SOTs can be generated from spin currents and concomitant spin accumulations at material boundaries, e.g., through spin Hall effects (SHE) in bulk materials [6–12] and directly from electric-current-generated spin accumulations, e.g., from interfacial Rashba-Edelstein effects [13–15]. Such spin source materials can be heavy metals such as Pt [8,16] and Ta [9], topological insulators [15], and Weyl semimetals such as WTe$_2$ [17,18]. Lately, there has been a growing interest in exotic in-plane FL torques, denoted as $\vec{\tau}_{FL}^z$, which are proportional to $\hat{m} \times \hat{z}$, as well as out-of-plane DL torques $\vec{\tau}_{DL}^z$ proportional to $\hat{m} \times (\hat{m} \times \hat{z})$, due to z-polarized spins (where z is the interface normal direction), which can deterministically switch magnetizations with directions $\hat{m}$ pointing out of plane without an external symmetry-breaking in-plane field. However, $\vec{\tau}_{FL}^z$ and $\vec{\tau}_{DL}^z$ are generally forbidden due to symmetry restrictions, but can be generated when the mirror symmetry in the plane perpendicular to the electric current direction is broken. Recent experiments have focused on exploring exotic SOTs generated from materials with intrinsically low symmetries, such as WTe$_2$/Permalloy (Py; Ni$_{80}$Fe$_{20}$) [17] and MnPd$_3$/CoFeB [19], and from materials systems with artificial symmetry breakings, such as strain-induced antisymmetry in NbSe$_2$/Py devices [20]. Nevertheless, many questions still remain open with respect to the exact mechanisms behind the generation of those exotic torques.

In this work, we studied the SOTs generated from magnetron-sputtered MoTe$_2$ films by using both spin-torque ferromagnetic resonance (ST-FMR) [8,9] and second harmonic Hall measurements [21,22]. We have observed sizable unconventional FL torques due to z-polarized spins ($\vec{\tau}_{FL}^z$) and x-polarized spins ($\vec{\tau}_{FL}^x \propto \hat{m} \times \hat{x}$), and DL torques due to z spins ($\vec{\tau}_{DL}^z$) in our MoTe$_2$/Py/MgO devices. To investigate the origins of these torques, we studied their thickness and current direction dependencies. Through careful crystal structure characterizations, we found our sputtered MoTe$_2$ has both preferential in- and out-of-plane alignments. We also found a strain in the MoTe$_2$ films, which could further reduce the symmetry and contribute to the presence of the exotic torques.

II. SAMPLE FABRICATION AND STRUCTURAL CHARACTERIZATION

We synthesized MoTe$_2$ films by magnetron cosputtering elemental Te and Mo targets onto A-plane sapphire (0.5-mm thick) substrates at temperatures ranging from 100–300 °C, followed by 1 h of annealing ranging from 350–500 °C in vacuum [23]. After the samples were cooled down, we deposited 10-nm Py and 2-nm MgO capping layer *in situ* before

*Contact author: sl117@illinois.edu
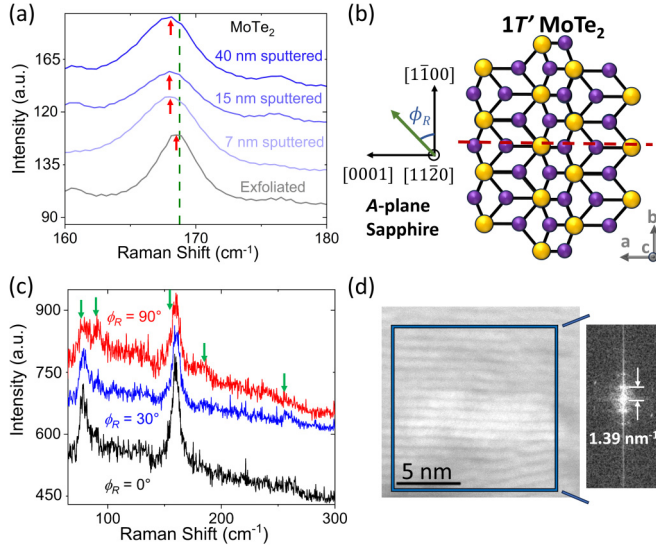†Contact author: axelh@illinois.edu

FIG. 1. (a) Raman spectra of magnetron-sputtered 40-nm (dark blue), 15-nm (blue), 7-nm (light blue), and exfoliated (gray) MoTe$_2$ samples. The spectra are shifted by an offset of 10 with respect to each other. The green dashed line and the red arrows indicate the theoretical and the measured MoTe$_2$ Raman shift position. (b) Crystal structure of 1T' MoTe$_2$ with the only mirror plane (red dashed line) along the a axis. On the left shows the A-plane sapphire substrate orientations. (c) Polarized Raman spectra for 15-nm MoTe$_2$/sapphire. A linearly polarized 633-nm light illuminates the sample with the polarization angle ϕ_R with respect to the [1$\bar{1}$00] direction of the A-plane sapphire substrate [shown in (b)]. $\phi_R = 0°$ means the polarization direction is parallel to the [1$\bar{1}$00] direction. The green arrows indicate different Raman modes and different peak intensities. (d) The STEM image of the sputtered MoTe$_2$ film and the fast Fourier transform of the blue circled area.

bringing the samples to ambient conditions. We performed x-ray diffraction (XRD) and scanning transmission electron microscopy (STEM) to characterize the sputtered MoTe$_2$ films. Figure 1(a) shows the Raman measurements on the sputtered MoTe$_2$ films and exfoliated 1T' MoTe$_2$ flakes (on A-plane sapphire), indicating the sputtered MoTe$_2$ to be 1T' phase, a monoclinic structure with a single mirror plane perpendicualr to b axis and parallel to ac plane [shown in Fig. 1(b)].

However, interestingly, for all MoTe$_2$ films (7 nm, 15 nm, and 40 nm) grown by magnetron sputtering, the characteristic Raman peak around 168 cm^{-1} shifted to lower energies compared to the same peak from the exfoliated 1T' MoTe$_2$ flake. Such a red shift of the Raman peak is generally caused by a strain from a tensile stress, which will lead to the elongation of the lattice and a decrease in the bond strength between neighboring atoms [24–26]. We think an in-plane strain with a perpendicular component to the mirror plane of 1T' MoTe$_2$ was induced during high-temperature processing, such that a red shift of 168 cm^{-1} Raman mode vibrating mostly in-plane perpendicular to the mirror plane of 1T' MoTe$_2$ [27] was observed across the samples. Figure 1(d) shows the STEM image of our sputtered 15-nm MoTe$_2$ sample. We calculated the distance between two adjacent bright fringes to be 1.39 nm^{-1} by performing the fast Fourier transform of the blue circled
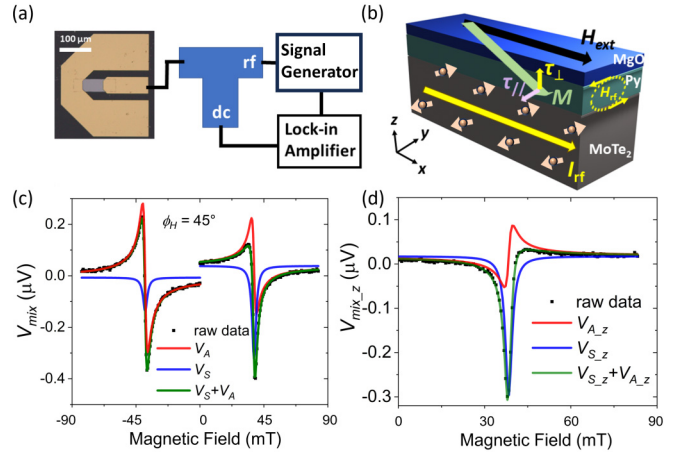

FIG. 2. (a) Diagram of our measurement setup for ST-FMR. A signal generator injects a GHz rf current whose amplitude is modulated by the reference signal of a lock-in amplifier into the device through the rf port of a bias tee. The mixing rf voltage is measured by the lock-in amplifier through the rf port of the bias tee. The dimension of the device is 80–130 μm in length and 20–40 μm in width. (b) A schematic of the spin-torque ferromagnetic resonance measurements on MoTe$_2$/Py/MgO devices. (c) The measured rf mixing voltages of sample 1 device 1 of MoTe$_2$(15)/Py/MgO at ϕ_H = 45° for positive and negative field scans. The power and frequency of the current is 4 dBm and 6 GHz, and the current direction is along [1$\bar{1}$00]. The fit for the mixing voltage is the green curve, which is the sum of V_S (blue) and V_A (red). (d) The mixing voltages $V_{\text{mix\_z}}$ with contributions solely from z-polarized spins, and we found $S_z = -0.313$ and $A_z = 0.140$, which are proportional to the sizes of $\vec{\tau}_{\text{FL}}^z$ and $\vec{\tau}_{\text{DL}}^z$.

area, which corresponds to 0.719 nm in real space and is close to the distance between the two MoTe$_2$ layers held by the van der Waals forces (0.693 nm), indicating the c axis of MoTe$_2$ is mostly aligned vertically. We further explored the in-plane orientation of MoTe$_2$ films to investigate if there is any preferential alignment with the A-plane sapphire substrate by using polarized Raman spectroscopy. We illuminated sputtered MoTe$_2$/sapphire samples with linearly polarized light at different ϕ_R, where ϕ_R is the angle between the polarization direction and the [1$\bar{1}$00] direction of the A-plane sapphire substrate. As shown in Fig. 1(c), the polarization-dependent Raman peaks and intensities (green arrows) demonstrate there is a crystallographic texture within the sputtered MoTe$_2$, with the a and b axis of the MoTe$_2$ being preferentially aligned along the [0001] and [1$\bar{1}$00] directions of the A-plane sapphire, respectively [5,28].

III. SPIN TRANSPORT MEASUREMENTS

A. Spin-torque ferromagnetic resonance

To study the characteristics of spin-orbit torques generated from sputtered MoTe$_2$ layer, we performed spin-torque ferromagnetic resonance (ST-FMR) measurements [8] on our MoTe$_2$(15)/Py(10)/MgO(2) devices (the individual layer thicknesses in parentheses are in nm). As indicated in Figs. 2(a) and 2(b), the samples were patterned and integrated into ground-signal-ground coplanar waveguides by ion

milling and lithography, and a radio-frequency (rf) current I_{rf} at 5–9 GHz along the $[1\bar{1}00]$ direction was applied through our devices with an external magnetic field H_{ext} sweeping in the xy plane from 0.1–0 T and from -0.1 T to 0 T. We then measured the resultant homodyne dc mixing voltages, V_{mix}, due to the coupling of the rf current and the anisotropic magnetoresistance (AMR) of Py modulated by SOTs from the MoTe$_2$ layer through a lock-in amplifier. Figure 2(c) shows the measured mixing voltages V_{mix} of device 1 for positive and negative field scans at $\phi_H = 45°$, where ϕ_H is the angle between the external magnetic field and the applied I_{rf} current. V_{mix} can be fitted by the sum of symmetric and antisymmetric Lorentzian functions

$$V_{\text{mix}} = S \frac{\Delta^2}{(H_{\text{ext}} - H_0)^2 + \Delta^2} + A \frac{\Delta(H_{\text{ext}} - H_0)}{(H_{\text{ext}} - H_0)^2 + \Delta^2}, \quad (1)$$

where H_{ext} is the applied field, H_0 is the ferromagnetic resonance field of permalloy, Δ is the half-width at half-maximum resonance linewidth, and S and A are the fitting parameters representing the sizes of the symmetric and antisymmetric Lorentzians V_S and V_A, which correspond to the sizes of the in-plane $\tau_\parallel$ and out-of-plane $\tau_\perp$ torques, respectively.

As shown in Fig. 2(c), the different line shapes of symmetric (V_S, blue) and antisymmetric (V_A, red) Lorentzians for positive and negative field scans indicate the presence of unconventional SOTs due to z-polarized spins. We added the mixing voltages measured from positive field and negative field scans, which cancels voltages contributed by spins polarized in-plane, while voltages due to spins polarized out of plane (along z) will add up constructively, due to their distinct symmetry characteristics in relation to the field direction [Eqs. (2) and (3)]. We then divided the added voltages by two and obtained the voltage ($V_{\text{mix\_z}}$), due to torques from z-polarized spins [Fig. 2(d)]. Through fitting $V_{\text{mix\_z}}$ using Eq. (1), we confirmed the existence of both $\vec{\tau}^z_{\text{DL}}$ and $\vec{\tau}^z_{\text{FL}}$ within device 1 of our MoTe$_2$(15)/Py(10)/MgO(2).

To extract different components of SOTs from $\tau_\parallel$ and $\tau_\perp$ that are related to V_S and V_A, we varied the angle ϕ_H between the current and field, and plot the extracted S and A as a function of angle ϕ_H. SOTs generated by x-, y-, and z-polarized spins have distinct angular dependencies for both S and A described by the following equations,

$$S = S^y_{\text{DL}} \sin(2\phi_H) \cos(\phi_H) + S^z_{\text{FL}} \sin(2\phi_H) + S^x_{\text{DL}} \sin(2\phi_H) \sin(\phi_H) \quad (2)$$

$$A = A^y_{\text{FL}} \sin(2\phi_H) \cos(\phi_H) + A^z_{\text{DL}} \sin(2\phi_H) + A^x_{\text{FL}} \sin(2\phi_H) \sin(\phi_H), \quad (3)$$

and we can obtain the sizes of $\vec{\tau}^y_{\text{DL}}$, $\vec{\tau}^z_{\text{FL}}$, $\vec{\tau}^x_{\text{DL}} \propto \hat{m} \times (\hat{m} \times \hat{x})$, $\vec{\tau}^y_{\text{FL}}$, $\vec{\tau}^z_{\text{DL}}$, and $\vec{\tau}^x_{\text{FL}}$ by fitting their angular dependencies using Eqs. (2) and (3), which are proportional to the fit values of S^y_{DL}, S^z_{FL}, S^x_{DL}, A^y_{FL}, A^z_{DL}, and A^x_{FL}, respectively.

As shown in Figs. 3(a) and 3(b), in device 1 of our MoTe$_2$(15)/Py/MgO sample, we found $A^y_{\text{FL}} = 0.624$, which we assume is mainly contributed by the Oersted field generated by the rf currents, and $S^y_{\text{DL}} = 0.155$, related to conventional $\vec{\tau}^y_{\text{DL}}$ in our sample. Also, we found $S^z_{\text{FL}} = -0.240$ and $A^z_{\text{DL}} = 0.104$, indicating sizable unconventional $\vec{\tau}^z_{\text{FL}}$ and $\vec{\tau}^z_{\text{DL}}$ due to z-polarized spins. In addition, we noticed that the
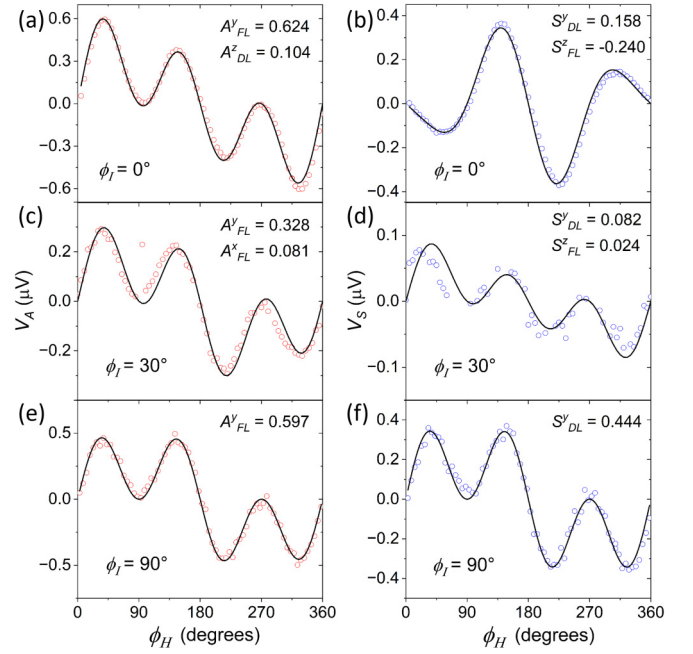

FIG. 3. (a), (c), and (e) Antisymmetric components V_A as a function of angle ϕ_H for $\phi_I = 0°$, $30°$, and $90°$. (b), (d), and (f) Symmetric components V_S as a function of angle ϕ_H for $\phi_I = 0°$, $30°$, and $90°$. The red and blue dots are extracted from the measured V_{mix}, and the black lines are the fitted curves using Eqs. (3) and (2).

polarity of $\vec{\tau}^z_{\text{FL}}$ is always opposite to that of $\vec{\tau}^z_{\text{DL}}$ for all the devices measured from MoTe$_2$(15)/Py/MgO. This indicates that the mechanisms behind the generation of the two torques are the same or are strongly correlated. The exact mechanism still remains unclear but this phenomenon has also been reported in the exfoliated single-crystalline $1T'$ MoTe$_2$/Py samples [5].

B. Current direction dependence

We studied the effects of crystallographic order on different torque components by applying the current at different angles ϕ_I through our MoTe$_2$(15)/Py devices, where ϕ_I is the angle between the current direction I and $[1\bar{1}00]$ of the A-plane substrate, with $\phi_I = 0°$ being I parallel to $[1\bar{1}00]$. As shown in Figs. 3(c) and 3(d), we found sizable $\vec{\tau}^x_{\text{FL}}$ due to x-polarized spins in the antisymmetric component when $\phi_I = 30°$, but no $\vec{\tau}^z_{\text{DL}}$ from the antisymmetric component. Moreover, we found the sizes of all unconventional torques diminished at $\phi_I = 90°$, and only the conventional torques $\vec{\tau}^y_{\text{DL}}$ remained [Figs. 3(e) and 3(f)].

The spin-orbit torque (SOT) efficiency quantifies the ability of the spin-orbit coupling to convert an applied electric current into a torque that influences the magnetization dynamics, and we calculated the SOT efficiencies ξ^y_{DL}, ξ^z_{FL}, and ξ^z_{DL} using the equation

$$\xi = \frac{\left(S^y_{\text{DL}}, S^z_{\text{FL}}, \text{ or } A^z_{\text{DL}}\right)}{A^y_{\text{FL}}} \frac{e\mu_0 M_S t d}{\hbar} [1 + M_{\text{eff}}/H_0]^{1/2}, \quad (4)$$

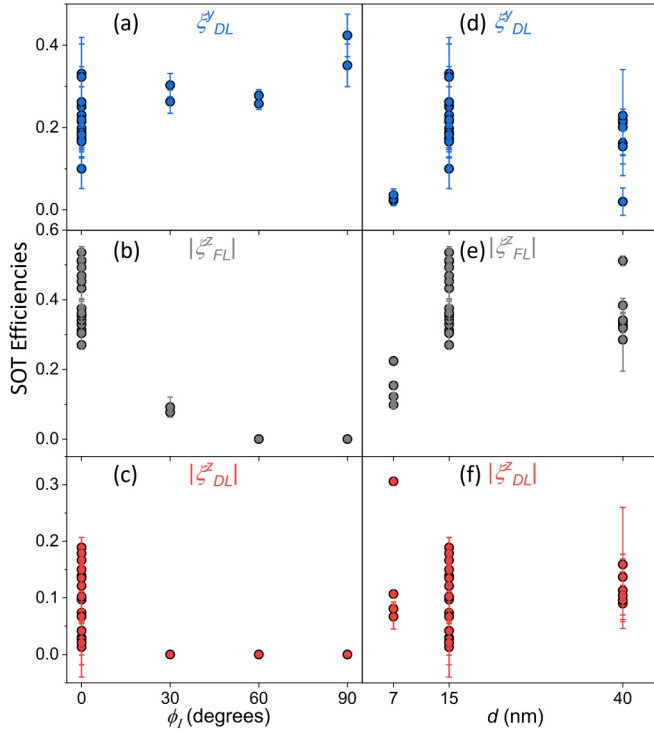where t and d are the thicknesses of Py and MoTe$_2$ layers, M_S is the saturation magnetization of Py, which is

FIG. 4. (a) ξ_{DL}^{y} at different ϕ_I, (b) and (c) are absolute values of ξ_{FL}^{z} and ξ_{DL}^{z} for better study the trend with respect to ϕ_I. (d), (e), and (f) are ξ_{DL}^{y}, $|\xi_{\text{FL}}^{z}|$, and $|\xi_{\text{DL}}^{z}|$ for devices with different MoTe$_2$ thicknesses (7, 15, and 40 nm).
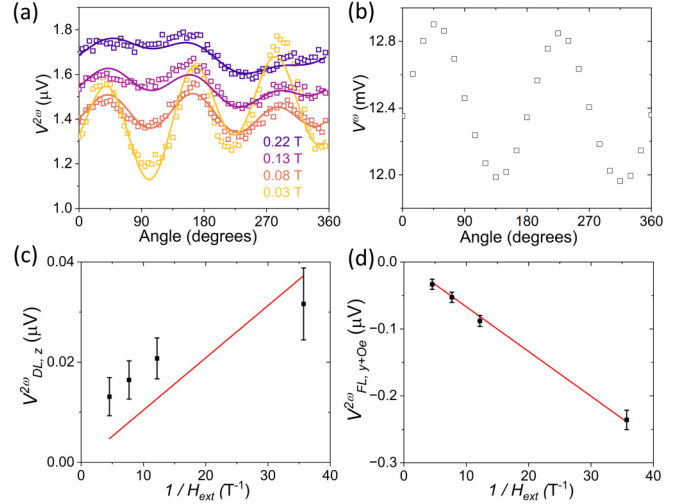

FIG. 5. (a) $V^{2\omega}$ (dots) of MoTe$_2$(15)/Py/MgO as a function of ϕ_H for various fields and the fit curves (lines) using Eq. (5). (b) V^{ω} as a function of ϕ_H under $H_{\text{ext}} = 0.22$ T. (c) and (d) Components of $V^{2\omega}$, $V_{\text{DL},z}^{2\omega}$, and $V_{\text{FL},y+\text{Oe}}^{2\omega}$, contributed by H_{DL}^{z} and $H_{\text{FL}}^{y} + H_{\text{Oe}}$, with linear fit red lines.

approximately $\mu_0 M_S \approx 0.8$ T. Figures 4(a)–4(c) show the calculated SOT efficiencies measured across different devices from MoTe$_2$(15)/Py/MgO heterostructures at different ϕ_I.

We found ξ_{DL}^{y} did not display a clear dependence on ϕ_I, whereas ξ_{FL}^{z} and ξ_{DL}^{z} both showed strong relations to current directions. When the current was applied at an angle to the $[1\bar{1}00]$ direction, ξ_{DL}^{z} vanished, while ξ_{FL}^{z} decreased at $\phi_I = 30°$ and diminished further at $\phi_I = 60°$ and $90°$. For ξ_{DL}^{z} and ξ_{FL}^{z}, the strong ϕ_I dependence indicates symmetry-related origin for the generation of $\vec{\tau}_{\text{DL}}^{z}$ and $\vec{\tau}_{\text{FL}}^{z}$, which would emerge when a current is applied perpendicular to the mirror plane of $1T'$ MoTe$_2$, and become symmetry forbidden when the current is applied along the mirror plane.

C. Thickness dependence

To better understand origins of different spin-orbit torque components, we investigated the thickness dependencies of different torques. Similarly, we performed ST-FMR measurements on MoTe$_2$(40 or 7)/Py/MgO heterostructures and calculated ξ_{DL}^{y}, ξ_{DL}^{z}, and ξ_{FL}^{z} using Eq. (4) for all the devices measured. As shown in Figs. 4(d)–4(f), ξ_{DL}^{y} and ξ_{FL}^{z} increased when the MoTe$_2$ thickness d increased from 7–15 nm, and became saturated when $d = 40$ nm, indicating possible origins to be bulk effects. The ϕ_I independence of ξ_{DL}^{y} suggests that $\vec{\tau}_{\text{DL}}^{y}$ originates from the spin Hall effect (SHE). We note that the magnitude of ξ_{DL}^{y} is comparable with results obtained previously with exfoliated MoTe$_2$ [29]. For ξ_{DL}^{z}, we did not observe any clear trend with respect to d [Fig. 4(f)], which would imply the origin of $\vec{\tau}_{\text{DL}}^{z}$ to be related to the interfacial

properties between MoTe$_2$ and Py. Finally, for MoTe$_2$(40) and MoTe$_2$(7), we found the polarities of ξ_{FL}^{z} and ξ_{DL}^{z} were always opposite for all the devices measured, just as what has been found in MoTe$_2$(15).

D. Second harmonic Hall measurements

Second harmonic Hall measurements are useful for analyzing in-plane $\tau_{\parallel}$ and out-of-plane $\tau_{\perp}$ spin-orbit torques, and can be complimentary to ST-FMR. For our MoTe$_2$(15)/Py/MgO sample, we applied a low-frequency ($\omega = 1131$ kHz) ac current with 4 mA amplitude along the x direction, with the magnetization of Py defined in plane by an external magnetic field (H_{ext}), and measured the transverse second harmonic Hall voltage $V^{2\omega}$ along y. $\tau_{\parallel}(\tau_{\perp})$ generated by MoTe$_2$ has an effective out-of-plane (in-plane) field that rotates the magnetization of Py out of plane (in plane) such that it modulates the change of the anomalous Hall resistance R_{AHE} (planar Hall resistance R_{PHE}) at a frequency ω of the ac current. The change of R_{AHE} and R_{PHE} couples to the applied current and gives rise to Hall voltages $V^{2\omega}$ on the second harmonic 2ω that can be detected through a lock-in amplifier. Figure 5(a) shows $V^{2\omega}$ as a function of ϕ_H, where ϕ_H is the angle between H_{ext} and the applied current, at various fields. For an in-plane magnetization system, different spin-orbit torque components can be extracted by their distinct angular dependencies described in the following equation [17,22,30],

$$V^{2\omega} = V_{\text{PHE}} \cos(2\phi_H) \left(\frac{H_{\text{FL}}^{y} + H_{Oe}}{H_{\text{ext}}} \cos(\phi_H) + \frac{H_{\text{FL}}^{x}}{H_{\text{ext}}} \sin(\phi_H) \right.$$
$$+ \frac{H_{\text{DL}}^{z}}{H_{\text{ext}}} \right) + \frac{1}{2} V_{\text{AHE}} \left(\frac{H_{\text{DL}}^{y}}{H_{\text{ext}} + H_k} \cos(\phi_H) \right.$$
$$\left. + \frac{H_{\text{DL}}^{x}}{H_{\text{ext}} + H_k} \sin(\phi_H) + \frac{H_{\text{FL}}^{z}}{H_{\text{ext}} + H_k} \right) + C, \quad (5)$$

where H_{FL}^y, H_{FL}^x, H_{DL}^z, H_{DL}^y, H_{DL}^x, and H_{FL}^z are the spin-orbit fields corresponding to the respective torques, and C is an offset constant. Through fitting, we observed sizable contributions from $\vec{\tau}_{FL}^y + \vec{\tau}_{Oe}$, $\vec{\tau}_{DL}^y$, and $\vec{\tau}_{DL}^z$ to $V^{2\omega}$, and plot the extracted components $V_{DL,z}^{2\omega}$ and $V_{FL,y+Oe}^{2\omega}$ as a function of $1/H_{ext}$ [see Figs. 5(c) and 5(d)]. Figure 5(b) shows the angular dependencies of the transverse V^ω, from which we derived the planar Hall effect (V_{PHE}) to be 0.45 mV. Thus, we calculated $H_{FL}^y + H_{Oe}$ and H_{DL}^z to be 8.0 A/m and 1.67 A/m. Finally, we calculated the SOT efficiency $\xi_{DL}^z = 0.068$ using

$$\xi_{DL}^z = \frac{2eM_s t_{FM}}{\hbar} \frac{H_{DL}^z}{J_{MoTe_2}}, \tag{6}$$

where e, t, and $\hbar$ are the electron charge, thickness of permalloy, and reduced Planck's constant. $J_{MoTe_2} = I_{MoTe_2}/(dw)$ is the current density flowing through the $MoTe_2$ layer, where I_{MoTe_2} is estimated to be 0.27 mA (see Supplemental Material [31]), $d = 15$ nm and $w = 20$ μm is the width of the device. We also estimated the Oersted field generated by I_{MoTe_2} to be 6.75 A/m using Ampere's law $H_{Oe} = I_{MoTe_2}/2w$ assuming the sample to be an infinitely wide plate. This confirms that the Oersted field dominates $V_{FL,y+Oe}^{2\omega}$.

IV. DISCUSSION

The observations of unconventional spin-orbit torques in magnetron-sputtered $1T'$ $MoTe_2$ films are possibly caused by two effects. First, as it can seen from Figs. 1(c) and 1(d), the sputtered $MoTe_2$ films have a textured structure with the c axis mostly aligned vertically and a (b) axis preferentially aligned along the $[0001]([1\bar{1}00])$ direction of the A-plane sapphire substrate, such that it preserves some macroscopic low symmetries that lack inversion symmetry and has only one mirror plane, enabling the generation of symmetry-forbidden SOTs when a current is applied at an angle to the mirror plane breaking this symmetry.

Second, a strain identified from the red shift of the 168 cm^{-1} Raman mode for all sputtered $MoTe_2$ films can further reduce the symmetry and enhance the effects generating unconventional spin-orbit torques. Such a strain can be caused by a tensile stress introduced by the mismatch between the thermal expansion coefficients of the substrates [32,33] and $MoTe_2$ during high-temperature growth. It is possible that the large SOT efficiency range in $1T'$ $MoTe_2$ films is caused by the relative alignment of the strain axis with the local grain orientations, analogous to the strain-induced $\vec{\tau}_{FL}^z$

found in single-crystalline $NbSe_2$ [20], and $\vec{\tau}_{DL}^z$ in exfoliated single-crystalline $1T'$ $MoTe_2$ [5].

Finally, we performed similar measurements on $1T'MoTe_2$ grown by metal-organic chemical vapor deposition [34,35], and observed different results (see Supplemental Material [31]).

V. CONCLUSION

In conclusion, we have studied and reported spin torques found in magnetron-sputtered $MoTe_2$/Py devices by performing ST-FMR and second harmonic Hall measurements on $MoTe_2$/Py(10)/MgO(2) samples. We explored the origins of different SOTs by studying the influence of the crystallographic order and the $MoTe_2$ thickness on the SOT efficiencies. Based on the ϕ_I and thickness d dependence of SOT efficiencies of different torques, the origins for $\vec{\tau}_{DL}^y$ and $\vec{\tau}_{FL}^z$ are probably due to bulk spin-orbit coupling, specifically the spin Hall effect for $\vec{\tau}_{DL}^y$. For $\vec{\tau}_{DL}^z$, the origins may be related to interfacial properties between the sputtered $MoTe_2$ films and the magnetic layer. Furthermore, the origins of $\vec{\tau}_{FL}^z$ and $\vec{\tau}_{DL}^z$ are closely related as their polarities are always opposite to each other. Our findings show that strains can be promising for generating large exotic in-plane FL and out-of-plane DL torques by introducing additional symmetry reduction, and single crystallinity is not necessary in generating exotic torques.

[1] A. Brataas, A. D. Kent, and H. Ohno, Current-induced torques in magnetic materials, Nature Mater. **11**, 372 (2012).

[2] M. Natsui, A. Tamakoshi, H. Honjo, T. Watanabe, T. Nasuno, C. Zhang, T. Tanigawa, H. Inoue, M. Niwa, T. Yoshiduka, Y. Noguchi, M. Yasuhira, Y. Ma, H. Shen, S. Fukami, H. Sato, S. Ikeda, H. Ohno, T. Endoh, and T. Hanyu, Dual-port SOT-MRAM achieving 90-MHz read and 60-MHz write operations under field-assistance-free condition, IEEE J. Solid-State Circuits **56**, 1116 (2021).

[3] Q. Shao, P. Li, L. Liu, H. Yang, S. Fukami, A. Razavi, H. Wu, K. Wang, F. Freimuth, Y. Mokrousov, M. D. Stiles, S. Emori, A. Hoffmann, J. Åkerman, K. Roy, J.-P. Wang, S.-H. Yang, K. Garello, and W. Zhang, Roadmap of spin-orbit torques, IEEE Trans. Magn. **57**, 1 (2021).

[4] A. Manchon, J. Železný, I. M. Miron, T. Jungwirth, J. Sinova, A. Thiaville, K. Garello, and P. Gambardella, Current-induced spin-orbit torques in ferromagnetic and antiferromagnetic systems, Rev. Mod. Phys. **91**, 035004 (2019).

[5] G. M. Stiehl, R. Li, V. Gupta, I. E. Baggari, S. Jiang, H. Xie, L. F. Kourkoutis, K. F. Mak, J. Shan, R. A. Buhrman, and D. C. Ralph, Layer-dependent spin-orbit torques generated by the centrosymmetric transition metal dichalcogenide $\beta - MoTe_2$, Phys. Rev. B **100**, 184402 (2019).

[6] S. Zhang, Spin Hall effect in the presence of spin diffusion, Phys. Rev. Lett. **85**, 393 (2000).

[7] J. Sinova, S. O. Valenzuela, J. Wunderlich, C. H. Back, and T. Jungwirth, Spin Hall effects, Rev. Mod. Phys. **87**, 1213 (2015).

[8] L. Liu, T. Moriyama, D. C. Ralph, and R. A. Buhrman, Spin-torque ferromagnetic resonance induced by the spin Hall effect, Phys. Rev. Lett. **106**, 036601 (2011).

[9] L. Liu, C.-F. Pai, Y. Li, H. W. Tseng, D. C. Ralph, and R. A. Buhrman, Spin-torque switching with the giant spin Hall effect of tantalum, Science **336**, 555 (2012).

[10] L. Liu, O. J. Lee, T. J. Gudmundsen, D. C. Ralph, and R. A. Buhrman, Current-induced switching of perpendicularly magnetized magnetic layers using spin torque from the spin Hall effect, Phys. Rev. Lett. **109**, 096602 (2012).

[11] A. Hoffmann, Spin Hall effects in metals, IEEE Trans. Magn. **49**, 5172 (2013).

[12] W. Zhang, J. Sklenar, B. Hsu, W. Jiang, M. B. Jungfleisch, J. Xiao, F. Y. Fradin, Y. Liu, J. E. Pearson, J. B. Ketterson, Z. Yang, and A. Hoffmann, Research update: Spin transfer torques in permalloy on monolayer MoS_2, APL Mater. **4**, 032302 (2016).

[13] Q. Shao, G. Yu, Y.-W. Lan, Y. Shi, M.-Y. Li, C. Zheng, X. Zhu, L.-J. Li, P. K. Amiri, and K. L. Wang, Strong Rashba-Edelstein effect-induced spin–orbit torques in monolayer transition metal dichalcogenide/ferromagnet bilayers, Nano Lett. **16**, 7514 (2016).

[14] S. Emori, T. Nan, A. M. Belkessam, X. Wang, A. D. Matyushov, C. J. Babroski, Y. Gao, H. Lin, and N. X. Sun, Interfacial spin-orbit torque without bulk spin-orbit coupling, Phys. Rev. B **93**, 180402(R) (2016).

[15] A. R. Mellnik, J. S. Lee, A. Richardella, J. L. Grab, P. J. Mintun, M. H. Fischer, A. Vaezi, A. Manchon, E.-A. Kim, N. Samarth, and D. C. Ralph, Spin-transfer torque generated by a topological insulator, Nature (London) **511**, 449 (2014).

[16] I. M. Miron, G. Gaudin, S. Auffret, B. Rodmacq, A. Schuhl, S. Pizzini, J. Vogel, and P. Gambardella, Current-driven spin torque induced by the Rashba effect in a ferromagnetic metal layer, Nature Mater. **9**, 230 (2010).

[17] D. MacNeill, G. M. Stiehl, M. H. D. Guimaraes, R. A. Buhrman, J. Park, and D. C. Ralph, Control of spin-orbit torques through crystal symmetry in WTe_2/ferromagnet bilayers, Nature Phys. **13**, 300 (2017).

[18] P. Li, W. Wu, Y. Wen, C. Zhang, J. Zhang, S. Zhang, Z. Yu, S. A. Yang, A. Manchon, and X.-x. Zhang, Spin-momentum locking and spin-orbit torques in magnetic nano-heterojunctions composed of Weyl semimetal WTe_2, Nature Commun. **9**, 3990 (2018).

[19] M. Dc, D.-F. Shao, V. D.-H. Hou, A. Vailionis, P. Quarterman, A. Habiboglu, M. B. Venuti, F. Xue, Y.-L. Huang, C.-M. Lee, M. Miura, B. Kirby, C. Bi, X. Li, Y. Deng, S.-J. Lin, W. Tsai, S. Eley, W.-G. Wang, J. A. Borchers *et al.*, Observation of anti-damping spin–orbit torques generated by in-plane and out-of-plane spin polarizations in $MnPd_3$, Nature Mater. **22**, 591 (2023).

[20] M. H. D. Guimarães, G. M. Stiehl, D. MacNeill, N. D. Reynolds, and D. C. Ralph, Spin–orbit torques in $NbSe_2$/permalloy bilayers, Nano Lett. **18**, 1311 (2018).

[21] C. O. Avci, K. Garello, M. Gabureac, A. Ghosh, A. Fuhrer, S. F. Alvarado, and P. Gambardella, Interplay of spin-orbit torque and thermoelectric effects in ferromagnet/normal-metal bilayers, Phys. Rev. B **90**, 224427 (2014).

[22] M. Hayashi, J. Kim, M. Yamanouchi, and H. Ohno, Quantitative characterization of the spin-orbit torque using harmonic Hall voltage measurements, Phys. Rev. B **89**, 144425 (2014).

[23] S. Pace, L. Martini, D. Convertino, D. H. Keum, S. Forti, S. Pezzini, F. Fabbri, V. Mišeikis, and C. Coletti, Synthesis of large-scale monolayer $1T'$-$MoTe_2$ and its stabilization via scalable hBN encapsulation, ACS Nano **15**, 4213 (2021).

[24] B. Karki, B. Freelon, M. Rajapakse, R. Musa, S. M. S. Riyadh, B. Morris, U. Abu, M. Yu, G. Sumanasekera, and J. B. Jasinski, Strain-induced vibrational properties of few layer black phosphorus and $MoTe_2$ via Raman spectroscopy, Nanotechn. **31**, 425707 (2020).

[25] T. Imajo, T. Suemasu, and K. Toko, Strain effects on polycrystalline germanium thin films, Sci. Rep. **11**, 8333 (2021).

[26] R. J. Angel, M. Murri, B. Mihailova, and M. Alvaro, Stress, strain and Raman shifts, Z. Kristallogr. Cryst. Mater. **234**, 129 (2019).

[27] X. Ma, P. Guo, C. Yi, Q. Yu, A. Zhang, J. Ji, Y. Tian, F. Jin, Y. Wang, K. Liu, T. Xia, Y. Shi, and Q. Zhang, Raman scattering in the transition-metal dichalcogenides of $1T'$-$MoTe_2$, T_d-$MoTe_2$, and T_d-WTe_2, Phys. Rev. B **94**, 214105 (2016).

[28] R. Beams, L. G. Cançado, S. Krylyuk, I. Kalish, B. Kalanyan, A. K. Singh, K. Choudhary, A. Bruma, P. M. Vora, F. Tavazza, A. V. Davydov, and S. J. Stranick, Characterization of few-layer $1T'$ $MoTe_2$ by polarization-resolved second harmonic generation and Raman scattering, ACS Nano **10**, 9626 (2016).

[29] S. Liang, S. Shi, C.-H. Hsu, K. Cai, Y. Wang, P. He, Y. Wu, V. M. Pereira, and H. Yang, Spin-orbit torque magnetization switching in $MoTe_2$/permalloy heterostructures, Adv. Mater. **32**, 2002799 (2020).

[30] O. Mosendz, J. E. Pearson, F. Y. Fradin, G. E. W. Bauer, S. D. Bader, and A. Hoffmann, Quantifying spin Hall angles from spin pumping: Experiments and theory, Phys. Rev. Lett. **104**, 046601 (2010).

[31] See Supplemental Material at http://link.aps.org/supplemental/10.1103/PhysRevB.110.024426 for further information regarding growth and characterization.

[32] S. Tian, Y. Yang, Z. Liu, C. Wang, R. Pan, C. Gu, and J. Li, Temperature-dependent Raman investigation on suspended graphene: Contribution from thermal expansion coefficient mismatch between graphene and substrate, Carbon **104**, 27 (2016).

[33] D. Yoon, Y.-W. Son, and H. Cheong, Negative thermal expansion coefficient of graphene measured by Raman spectroscopy, Nano Lett. **11**, 3227 (2011).

[34] S. T. Chyczewski, H. Lee, S. Li, M. Eladl, J.-F. Zheng, A. Hoffmann, and W. Zhu, Strong damping-like torques in wafer-scale $MoTe_2$ grown by MOCVD, arXiv:2404.19135.

[35] T. A. Empante, Y. Zhou, V. Klee, A. E. Nguyen, I. H. Lu, M. D. Valentin, S. A. N. Alvillar, E. Preciado, A. J. Berges, C. S. Merida, M. Gomez, S. Bobek, M. Isarraraz, E. J. Reed, and L. Bartels, Chemical vapor deposition growth of few-layer $MoTe_2$ in the 2H, $1T'$, and 1T phases: Tunable properties of $MoTe_2$ films, ACS Nano **11**, 900 (2017).